Estimation of the NiCu Cycle Strength and Its Impact on Type I X-Ray Bursts

Chanhee Kim[1] , Kyungyuk Chae[1] , Soomi Cha[2], Kyujin Kwak[3] , Gwangeon Seong[3], and Michael Smith[4]
[1] Department of Physics, Sungkyunkwan University, Suwon 16419, Republic of Korea; kchae@skku.edu
[2] Center for Exotic Nuclear Studies, Institute for Basic Science (IBS), Daejeon 34126, Republic of Korea
[3] Department of Physics, School of Natural Science, Ulsan National Institute of Science and Technology (UNIST), Ulsan 44919, Republic of Korea
[4] Physics Division, Oak Ridge National Laboratory, Oak Ridge, TN 37831, USA
Received 2022 January 26; revised 2022 March 16; accepted 2022 March 16; published 2022 April 15

Abstract

Type I X-ray bursts (XRBs) are powered by thermonuclear burning on proton-rich unstable nuclides. The construction of burst models with accurate knowledge of nuclear physics is required to properly interpret burst observations. Numerous studies that have investigated the sensitivities of burst models to nuclear inputs have commonly extracted the strength of the NiCu cycle in the rp process, determined by the $^{59}Cu(p,\alpha)^{56}Ni$ and $^{59}Cu(p,\gamma)^{60}Zn$ thermonuclear reaction rates, as critical in the determination of reaction flow in the burst. In this study, the strength of the cycle at the XRB temperature range was estimated based on published experimental data. The nuclear properties of the compound nucleus ^{60}Zn were evaluated for the $^{59}Cu(p,\alpha)^{56}Ni$ and $^{59}Cu(p,\gamma)^{60}Zn$ reaction rate calculations. Monte Carlo rate calculations were conducted to include the large uncertainties of nuclear properties in the calculations. In the current work, a weak NiCu cycle is expected, whereas the rates adopted by the previous studies suggest a strong NiCu cycle. Model simulations were performed with the new rates to assess the impact on Type I XRBs. The results show that the estimated cycle strength does not strongly influence the model predictions of the burst light curve or synthesized abundances.

1. Introduction

Type I X-ray bursts (XRBs) are explosive astrophysical events, caused by thermonuclear runaways on the surfaces of neutron stars in low-mass X-ray binary systems (Woosley & Taam 1976; Joss 1977; Wallace & Woosley 1981; Lewin et al. 1993; Schatz & Rehm 2006; Parikh et al. 2013). XRBs have been extensively studied with regard to their influence on the properties of neutron stars, binary systems, and potentially galactic abundances (Lewin et al. 1993; Woosley et al. 2004; Weinberg et al. 2006; Parikh et al. 2008, 2013). The bursts are driven by nucleosynthesis processes, mainly the 3α reaction, αp process, and rapid proton capture (rp) process (Wallace & Woosley 1981; van Wormer et al. 1994; Woosley et al. 2004; Parikh et al. 2013). These processes involve hundreds of proton-rich unstable isotopes with thousands of nuclear reactions. To construct precise models of XRB nucleosynthesis, the best determination of nuclear reaction rates, masses, and β decay rates must be utilized. Predictions of light curves and burst ashes by the models are highly sensitive to the input nuclear physics (Woosley et al. 2004; Parikh et al. 2008; Cyburt et al. 2010, 2016; Meisel et al. 2019).

Numerous studies have investigated the sensitivity of XRB models to nuclear inputs (Parikh et al. 2008, 2009; Cyburt et al. 2016; Schatz & Ong 2017; Meisel et al. 2019). In particular, nuclear reaction rates have been the focus as most of them are not experimentally known and have large uncertainties. Parikh et al. (2008), Cyburt et al. (2016), and Meisel et al. (2019) all identified that variations of the $^{59}Cu(p,\alpha)^{56}Ni$ and $^{59}Cu(p,\gamma)^{60}Zn$ reaction rates significantly affect the properties of light curves and composition of burst ashes. These two reactions compete with each other in the NiCu cycle in the rp process,

$^{56}Ni(p,\gamma)^{57}Cu(p,\gamma)^{58}Zn(\beta^+\nu)^{58}Cu(p,\gamma)^{59}Zn(\beta^+\nu)^{59}Cu(p,\alpha)^{56}Ni$, determining the strength of the cycle (van Wormer et al. 1994). The $^{59}Cu(p,\alpha)^{56}Ni$ reaction takes the reaction flow back to the beginning of the NiCu cycle, whereas the $^{59}Cu(p,\gamma)^{60}Zn$ reaction takes the flow out of the cycle and up to higher mass nuclides. The two rates are currently estimated by a statistical model with the code NON-SMOKER (Rauscher & Thielemann 2000; Cyburt et al. 2010). Three sensitivity studies (Parikh et al. 2008; Cyburt et al. 2016; Meisel et al. 2019), showed that a high $^{59}Cu(p,\alpha)^{56}Ni$ reaction rate or a low $^{59}Cu(p,\gamma)^{60}Zn$ reaction rate leads to considerable changes in the model predictions, where these variations create a strong NiCu cycle that impedes the synthesis of heavier nuclei.

In this study, the strength of the NiCu cycle in the temperature range relevant to XRBs was estimated using experimental data from previous measurements. The nuclear properties of the compound nucleus ^{60}Zn were assessed using the published data (Greenfield et al. 1972; Pougheon et al. 1972; Winsborrow & Macefield 1972; Evers et al. 1974; Alford et al. 1975; Weber et al. 1979; Schubank et al. 1989; Boucenna et al. 1990; de Angelis et al. 1998; Svensson et al. 1999; Mazzocchi et al. 2001). A Monte Carlo technique was implemented to determine the $^{59}Cu(p,\alpha)^{56}Ni$ and $^{59}Cu(p,\gamma)^{60}Zn$ thermonuclear reaction rates and their uncertainties from the uncertainties of the nuclear properties. The estimated rates were used as inputs to Type I XRB models using the MESA code (Paxton et al. 2015). The impact of the estimated NiCu cycle strength and its uncertainty on the XRB light curves and nucleosynthesis was investigated.

2. Nuclear Properties of ^{60}Zn

2.1. Energy Levels

Measurements, including those of Greenfield et al. (1972), Pougheon et al. (1972), Winsborrow & Macefield (1972), Evers et al. (1974), Alford et al. (1975), Weber et al. (1979),

Schubank et al. (1989), Boucenna et al. (1990), de Angelis et al. (1998), and Svensson et al. (1999), have found numerous ^{60}Zn levels above the proton threshold (S_p = 5105 keV) (Wang et al. 2021). Based on the latest information, we have done a careful reassessment of the excitation energies derived from nucleon transfer reactions. These include ^{58}Ni(^{3}He,n)^{60}Zn (Greenfield et al. 1972; Winsborrow & Macefield 1972; Evers et al. 1974; Alford et al. 1975), ^{58}Ni(^{12}C,^{10}Be)^{60}Zn (Weber et al. 1979; Boucenna et al. 1990), and ^{58}Ni(^{16}O,^{14}C)^{60}Zn (Pougheon et al. 1972).

Two processes were used for the reassessment. First, the masses used in the reaction kinematic calculations were replaced with the most recently evaluated values from the 2020 Atomic Mass Evaluation (Wang et al. 2021). The energy levels were recalculated using the updated masses. Second, excitation energies from precise energy level measurements by Schubank et al. (1989), Svensson et al. (1999), and Mazzocchi et al. (2001) were used as calibration points. For the levels measured by more than one study, weighted averages with their uncertainties were used. The weighted average and its uncertainty are defined by

$$\overline{E}_{\text{weighted}} = \frac{\sum_i E_i \cdot \sigma_i^{-2}}{\sum_i \sigma_i^{-2}} \qquad (1)$$

and

$$\sigma_{\text{weighted}} = \frac{1}{\sqrt{\sum_i \sigma_i^{-2}}}, \qquad (2)$$

where E and σ represent the value taken to obtain the average and its uncertainty, respectively. The energy levels from the other studies were calibrated to the newly obtained set of levels. Calibration points were chosen best to enclose the energy region of interest. Figure 1 shows the total adjustment by the above processes for each reported energy level. The adjustments are mostly higher than 10 keV and agree with the uncertainties presented in each paper.

Winsborrow & Macefield (1972) (^{58}Ni(^{3}He,n)^{60}Zn) reported energy levels with large uncertainties, approximately 0.2 MeV for each energy level. Two of the adjusted energy levels, E_x = 6.886 and 7.476 MeV, have approximately the same values as the levels of E_x = 6.923 and 7.469 MeV measured by Boucenna et al. (1990) and de Angelis et al. (1998), respectively. However, the two energy states were assigned at the same levels as E_x = 6.638 and 7.371 MeV because other measurements used the ^{58}Ni(^{3}He,n)^{60}Zn reaction agree well each other at 6.638 and 7.371 MeV, including the work of Alford et al. (1975), in which the same beam energy was used (15 MeV).

For the states observed in multiple studies, the weighted averages of the adjusted levels with their uncertainties were used. The evaluated energy levels in ^{60}Zn, resonance energies of the reactions, and their uncertainties are summarized in Table 1. It covers a range of energy levels from right above the proton threshold to $E_x \sim$ 8 MeV, which contains the energy region for the ^{59}Cu(p,α)^{56}Ni and ^{59}Cu(p,γ)^{60}Zn reactions relevant to the temperature of XRBs. The resonance energies were calculated by subtracting the proton threshold from the energy levels (Wang et al. 2021). Energy levels listed in the previous compilation of A = 60 (Browne & Tuli 2013), are also presented in Table 1. The compilation does not include the work of de Angelis et al. (1998). Additionally, in the present work, the level of E_x = 5.300 MeV from the compilation was considered the same as the level of E_x = 5.292 MeV.
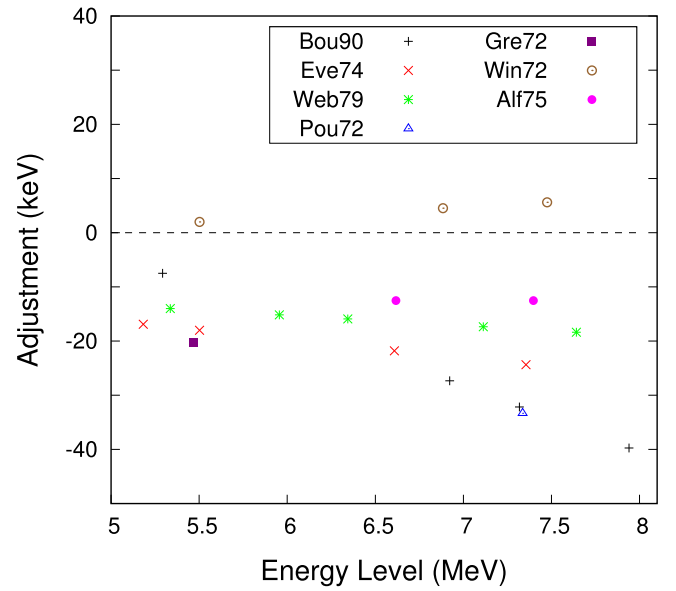

Figure 1. Adjustments to the excitation energies measured by the references that implemented nucleon transfer reactions. The references are presented by the first three letters of the first author's last name combined with the last two numbers of the publication year.

Table 1
Energy Levels in ^{60}Zn above the Proton Threshold, Resonance Energies, Uncertainties in Kiloelectronvolts and Corresponding References

Previous[a]	Present		
E_x	E_x	E_{res}	References
5200(60)	5183(60)	78	Eve74
5292(1)	5292(1)	187	Bou90, deA98, Sve99
5300(50)			
5337(1)	5336(4)	231	Web79, Sch89
	5369(2)	264	deA98
5504(1)	5502(2)	397	Win72, Gre72, Eve74, Sch89
	5729(3)	624	deA98
5970(70)	5955(70)	850	Web79
6360(70)	6344(70)	1239	Web79
6639(1)	6638(3)	1533	Win72, Eve74, Alf75, Sch89
6950(50)	6923(50)	1815	Bou90
7130(70)	7113(70)	2008	Web79
7373(2)	7318(50)	2213	Bou90
7380(30)	7371(4)	2265	Win72, Pou72, Eve74, Alf75, Sch89
	7469(4)	2364	deA98
7660(70)	7642(70)	2537	Web79
7980(50)	7940(50)	2835	Bou90

Notes. Energy levels from the previous compilation of Browne & Tuli (2013) are also presented.
[a] Browne & Tuli (2013).

The uncertainties of the ^{60}Zn resonance energies produce uncertainties in the ^{59}Cu(p,α)^{56}Ni and ^{59}Cu(p,γ)^{60}Zn thermonuclear reaction rates. Because the contribution of each resonance to the total rate depends exponentially on the resonance energy, even small uncertainties can make significant differences in the rate. Monte Carlo samplings for each resonance energy were performed to include the uncertainties. A probability density function for each energy state was chosen to be a Gaussian function with a mean and standard deviation as the energy value and its uncertainty, respectively (Longland

et al. 2010). For the state at $E_x = 5.183$ MeV with a large uncertainty, a cutoff was applied to the tails of the Gaussian function to ensure that the sampled energies are above the proton threshold. The effect of a subthreshold resonance was not considered because its contribution to a reaction rate at high XRB temperatures is mostly negligible.

2.2. Spins

The spin parities of the states in ^{60}Zn have also been studied in the previous measurements, mostly focusing on low-lying states (Greenfield et al. 1972; Pougheon et al. 1972; Winsborrow & Macefield 1972; Evers et al. 1974; Kamermans et al. 1974; Alford et al. 1975; Weber et al. 1979; Schubank et al. 1989; Boucenna et al. 1990; de Angelis et al. 1998; Svensson et al. 1999; Mazzocchi et al. 2001). For high energy states above the proton threshold, only a few studies have been conducted on each energy state, but there are frequent discrepancies in those measurements. There are, however, consistent assignments for the two states at $E_x = 6.638$ and 7.371 MeV. The ^{58}Ni(^{3}He,n)^{60}Zn studies of Winsborrow & Macefield (1972), Evers et al. (1974), and Alford et al. (1975) reported that the excited state at 6.638 MeV has 0^+ spin parity. Except for one outlier study Schubank et al. (1989), several ^{58}Ni(^{3}He,n)^{60}Zn measurements found the spin parity of the state at $E_x = 7.371$ MeV to be $J^\pi = 0^+$ (Winsborrow & Macefield 1972; Pougheon et al. 1972; Evers et al. 1974; Alford et al. 1975). Pougheon et al. (1972) claimed that the state is the $T = 2$ isobaric analog state of ^{60}Ni at the ground state through the ^{58}Ni(^{3}He,n)^{60}Zn measurement, which results in $J^\pi = 0^+$. For the other states, there is either no agreement or no measurements of the spin parities.

Spin distributions from the Fermi gas model (Gilbert & Cameron 1965; Koning et al. 2017) were implemented for the unknown spins. Level density models based on this model are widely utilized for nuclei in the intermediate mass range and beyond (Garrett et al. 2001; Schiller et al. 2001; Long et al. 2017, 2018; Rahman & Zubair 2020; Özdoğan et al. 2021). The spin distribution function can be written as

$$R_{\mathrm{Fermi}}(E_x, J) = \frac{2J + 1}{2\sigma^2} \exp\left[-\frac{\left(J + \frac{1}{2}\right)^2}{2\sigma^2}\right]. \qquad (3)$$

Here, E_x is the excitation energy, J is the spin of the level, and σ^2 is the spin cutoff parameter. The function can be obtained by factorizing the Fermi gas level density expression. The spin cutoff parameter was adopted from the TALYS 1.9 Manual (Koning et al. 2017), using level density parameters from the backshifted Fermi gas model. Figure 2 shows the spin distributions for the states at $E_x = 5.502$ and 7.371 MeV as examples. Monte Carlo sampling was conducted using this function. Meanwhile, unknown parities were randomly sampled with the equiparity assumption.

2.3. Partial Widths

The particle partial width for a given level λ and channel c is defined by (Lane & Thomas 1958)

$$\Gamma_{\lambda c} = 2\frac{\hbar^2}{mR^2}P_c\theta_{\lambda c}^2, \qquad (4)$$
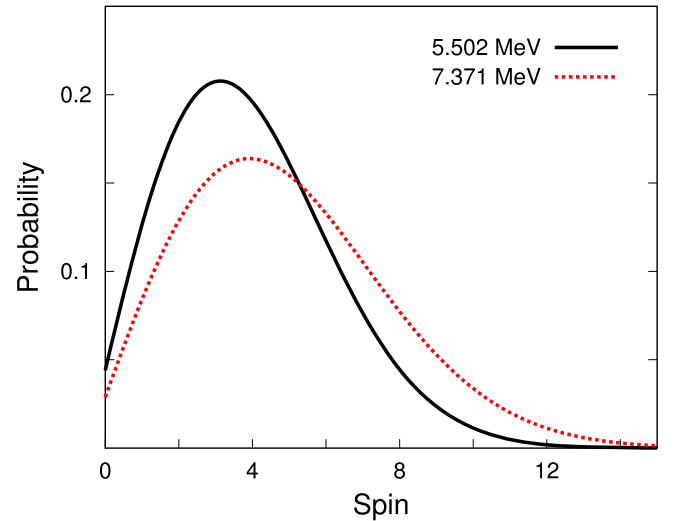

Figure 2. Examples of spin distributions used for the Monte Carlo samplings. The states at $E_x = 5.502$ and 7.371 MeV are plotted as representatives.

where m is the reduced mass of the interacting nuclei, R is the interaction radius, P_c is the penetration factor, and $\theta_{\lambda c}^2$ is the dimensionless reduced width. $\theta_{\lambda c}^2$ can be given as (Iliadis 1997; Longland et al. 2010),

$$\theta_{\lambda c}^2 = C^2S\theta_{\mathrm{sp}}^2, \qquad (5)$$

where C^2S is the spectroscopic factor, and θ_{sp}^2 is the dimensionless single-particle reduced width. The proton partial widths were calculated for each resonance in Table 1 using Equations (4) and (5). The interaction radius (in femtometers) was chosen as $R = 1.25(A_t^{1/3} + A_p^{1/3})$, where A_t and A_p represent the target and projectile mass numbers, respectively.

The nuclear properties related to the proton partial widths of ^{60}Zn have not been measured before. Here, the spectroscopic factors were estimated using the shell model calculations. The interaction presented by Honma et al. (2009), was implemented using the code KSHELL (Shimizu 2013; Shimizu et al. 2019). The calculated states, along with their spectroscopic factors (C^2S_{shell}), by the shell model are challenging to match with the evaluated energy states in Table 1. Gaussian-weighted averages of C^2S_{shell} were used for the spectroscopic factor (C^2S) of each evaluated state, as was similarly done in Long et al. (2017) and Long et al. (2018). The following expression shows a Gaussian-weighted average of C^2S_{shell}:

$$C^2S = \frac{\sum_{\mathrm{shell}}[C^2S_{\mathrm{shell}} \cdot G(E_{\mathrm{shell}})]}{\sum_{\mathrm{shell}}G(E_{\mathrm{shell}})} \qquad (6)$$

with

$$G(E_{\mathrm{shell}}) = \frac{1}{\sqrt{2\pi}\,\sigma}e^{-(E_{\mathrm{shell}}-E_x)^2/(2\sigma^2)}. \qquad (7)$$

E_{shell} is the excitation energy calculated by the shell model. E_x and σ are the energy of the evaluated state and its uncertainty, respectively. If the difference between E_{shell} and E_x is large, the weight for the corresponding C^2S_{shell} will be small, as it is determined by the Gaussian function centered at E_x; the opposite occurs if the difference is small. C^2S for each energy state was estimated as the average of the weighted C^2S_{shell}.

3

Table 2
Information on Possible Final States in ^{56}Ni after α Transitions from ^{60}Zn

E_x[a] (MeV)	$J^{\pi a}$	Q-value (MeV)[b]
g. s	0^+	2.6918
2.7006(7)	2^+	5.3924
3.9236(13)	4^+	6.6154
3.9566(13)	0^+	6.6484

Notes. The reaction Q-values for ^{56}Ni + $\alpha \rightarrow {}^{60}$Zn are also presented.
[a] Junde et al. (2011).
[b] Wang et al. (2021).

The proton dimensionless single-particle reduced width, $\theta^2_{\rm sp}$, was adopted from Iliadis (1997). The work presents fitting results on calculated $\theta^2_{\rm sp}$ for target masses $A = 12$–50, bombarding energy $E \leqslant 1000$ keV, and orbits $nl = 2s$, $2p$, $1d$, and $1f$. In the current work, the following assumptions were adopted. First, the target masses and bombarding energies can be extended to $A = 59$ and $E \leqslant 2900$ keV. Second, the $\theta^2_{\rm sp}$ values for the $1g$ orbit can be approximated to those for $1f$, which was demanded as the shell model space includes the orbit $1g_{9/2}$ (Honma et al. 2009).

The α widths were estimated using Equation (4). The Porter–Thomas distribution was implemented to obtain the dimensionless reduced widths, $\theta^2_{\lambda c}$, as the shell model calculation is challenging for the α transition. The distribution can be expressed as (Porter & Thomas 1956; Longland et al. 2010; Pogrebnyak et al. 2013)

$$f_{\rm PT}(\theta^2) = \frac{C}{\sqrt{\theta^2}} e^{-\theta^2/2\langle\theta^2\rangle} , \qquad (8)$$

where C is a normalization constant, θ^2 is the dimensionless reduced width, and $\langle\theta^2\rangle$ is the mean value of θ^2. The required parameter, $\langle\theta^2\rangle$, was obtained from Pogrebnyak et al. (2013). They extracted the mean α reduced widths from experimental data covering the range of $A = 28$–40. The average of the mean reduced widths, $\langle\theta^2_\alpha\rangle = 0.018 \pm 0.002$, was adopted, assuming that the result can be extended to $A = 60$. The distribution was used for the Monte Carlo sampling of the α dimensionless reduced widths.

l-values for the α penetration factors were obtained by applying the selection rules to the transitions between the deduced spin parities in Section 2.2 and the spin parities of possible final states in ^{56}Ni. The possible final states for the ^{59}Cu$(p,\alpha)^{56}$Ni reaction were determined by the states presented in Junde et al. (2011) and Q-values (Wang et al. 2021). Table 2 summarizes the adopted states in ^{56}Ni with spin parities and Q-values.

The γ-ray partial width for the l-pole is given by (Weisskopf & Blatt 1954; Iliadis 2015),

$$\Gamma_\gamma(\sigma l) = \frac{8\pi(l+1)}{l[(2l+1)!!]^2}\left(\frac{E_\gamma}{\hbar c}\right)^{2l+1} B(\sigma l), \qquad (9)$$

where σ represents either electric or magnetic radiation, E_γ is the radiation energy, and $B(\sigma l)$ is the reduced transition probability. The γ-ray widths have not been experimentally studied also. The estimations were also based on the same shell model calculation used to obtain the proton widths (Honma et al. 2009). As there is the same matching issue mentioned above, the Gaussian-weighted averages of the reduced

Table 3
Γ_p and Γ_γ Adopted in This Work

E_x (keV)	Γ_p (eV)	Γ_γ (eV)
5183(60)	2.499×10^{-35}	5.439×10^{-3}
5292(1)	9.977×10^{-20}	4.831×10^{-4}
5336(4)	5.810×10^{-15}	4.164×10^{-4}
5369(2)	2.461×10^{-13}	2.478×10^{-4}
5502(2)	6.716×10^{-9}	4.629×10^{-1}
5729(3)	1.383×10^{-7}	3.996×10^{-3}
5955(70)	1.760×10^{-3}	2.954×10^{-1}
6344(70)	5.579×10^{-1}	5.482×10^{-1}
6638(3)	4.015	3.587×10^{-2}
6923(50)	1.270×10^{1}	2.097×10^{-2}
7113(70)	3.898×10^{1}	4.102×10^{-2}
7318(50)	2.875×10^{1}	7.888×10^{-2}
7371(4)	3.561×10^{1}	1.850×10^{-2}
7469(4)	4.939×10^{-2}	6.561×10^{-4}
7642(70)	7.689×10^{1}	6.232×10^{-4}
7940(50)	1.465×10^{2}	1.172×10^{-4}

Note. The presented Γ_p were calculated using the mean values of the Gaussian functions, which are the probability density functions for the resonance energies. See the text for more details.

transition probabilities from the shell model were used to calculate the widths.

A summary of the Γ_p and Γ_γ is in Table 3. Note that the Γ_p are affected by the resonance energies sampled from their probability density functions for each iteration of the Monte Carlo reaction rate calculations (see Section 3). The sampled resonance energies were used to calculate the proton penetration factors and dimensionless single-particle reduced widths. The Γ_p presented in Table 3 were calculated using the mean values of the probability density functions, which are the Gaussian functions (see Section 2.1). For the Γ_α, note that not only the distributions of the resonance energies, the spin distributions and Porter–Thomas distribution were also used to calculate the Γ_α for each iteration. As both are asymmetric distributions, it is challenging to find representative values for the Γ_α.[5]

3. Monte Carlo Reaction Rate Calculations

As the reported energy levels in the compound nucleus ^{60}Zn are isolated (i.e., non-overlapping) as can be seen in Table 1, we implemented the narrow resonance formalism for the reaction rate calculations, assuming the resonance contribution will dominate over the other contributions such as direct capture into bound levels. The rate calculations of the ^{59}Cu$(p,\alpha)^{56}$Ni and ^{59}Cu$(p,\gamma)^{60}$Zn reactions were performed in the temperature range of 0.1–2.0 GK. The reaction rate in units of cubic centimeters per mole per second can be expressed as

$$N_A\langle\sigma v\rangle_r = 1.5399 \times 10^{11} \cdot T_9^{-3/2}\left(\frac{M_0 + M_1}{M_0 M_1}\right)^{3/2}$$

$$\cdot \sum_r (\omega\gamma)_r e^{-11.605 E_r/T_9} \qquad (10)$$

---

[5] Additionally, the sampled spins nonlinearly affect the widths as they will determine l-values of the transitions.
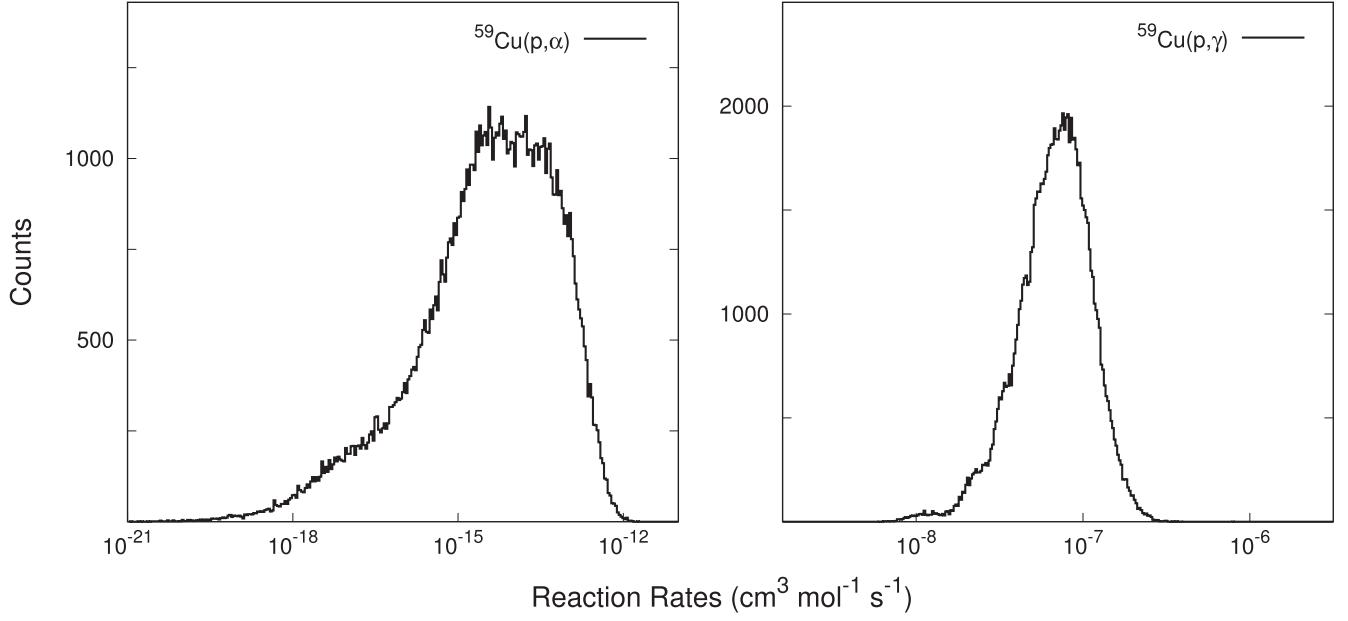
Figure 3. Obtained histograms of the ^{59}Cu$(p,\alpha)^{56}$Ni and ^{59}Cu$(p,\gamma)^{60}$Zn reaction rates through the Monte Carlo calculations at $T_9 = 0.4$.

Table 4
Estimated Thermonuclear Reaction Rates, $N_A\langle\sigma v\rangle$, for the ^{59}Cu$(p,\alpha)^{56}$Ni and ^{59}Cu$(p,\gamma)^{60}$Zn Reactions in Units of Cubic Centimeters per Mole per Second

	^{59}Cu$(p,\alpha)^{56}$Ni			^{59}Cu$(p,\gamma)^{60}$Zn		
T_9 (GK)	Low Rate	Median Rate	High Rate	Low Rate	Median Rate	High Rate
0.1	4.25×10^{-31}	2.80×10^{-26}	8.27×10^{-24}	6.03×10^{-20}	1.26×10^{-19}	2.16×10^{-19}
0.2	3.06×10^{-23}	3.26×10^{-20}	1.30×10^{-17}	4.76×10^{-13}	1.26×10^{-12}	2.54×10^{-12}
0.3	3.26×10^{-19}	2.92×10^{-17}	1.60×10^{-15}	5.04×10^{-10}	1.36×10^{-9}	2.88×10^{-9}
0.4	4.50×10^{-17}	4.27×10^{-15}	7.02×10^{-13}	2.62×10^{-8}	6.80×10^{-8}	1.39×10^{-7}
0.5	8.44×10^{-15}	3.59×10^{-13}	6.55×10^{-11}	8.32×10^{-7}	2.45×10^{-6}	5.76×10^{-6}
0.6	9.40×10^{-13}	1.44×10^{-11}	1.89×10^{-9}	1.68×10^{-5}	4.88×10^{-5}	9.90×10^{-5}
0.7	3.33×10^{-11}	3.70×10^{-10}	3.17×10^{-8}	1.68×10^{-4}	4.71×10^{-4}	9.20×10^{-4}
0.8	5.04×10^{-10}	5.16×10^{-9}	2.98×10^{-7}	1.06×10^{-3}	2.82×10^{-3}	5.72×10^{-3}
0.9	4.62×10^{-9}	4.32×10^{-8}	1.86×10^{-6}	4.68×10^{-3}	1.22×10^{-2}	2.56×10^{-2}
1.0	3.02×10^{-8}	2.46×10^{-7}	7.61×10^{-6}	1.57×10^{-2}	4.15×10^{-2}	8.89×10^{-2}
1.1	1.47×10^{-7}	1.06×10^{-6}	2.57×10^{-5}	4.25×10^{-2}	1.16×10^{-1}	2.48×10^{-1}
1.2	5.84×10^{-7}	3.68×10^{-6}	7.24×10^{-5}	9.87×10^{-2}	2.76×10^{-1}	5.90×10^{-1}
1.3	1.95×10^{-6}	1.08×10^{-5}	1.64×10^{-4}	2.02×10^{-1}	5.81×10^{-1}	1.23
1.4	5.73×10^{-6}	2.77×10^{-5}	3.56×10^{-4}	3.79×10^{-1}	1.10	2.30
1.5	1.44×10^{-5}	6.47×10^{-5}	7.12×10^{-4}	6.53×10^{-1}	1.92	3.98
2.0	3.96×10^{-4}	1.49×10^{-3}	1.24×10^{-2}	4.41	1.31×10^1	2.60×10^1

Note. The low and high rates were extracted at a 90% confidence level.

with

$$\omega\gamma = \frac{2J + 1}{(2j_p + 1)(2j_t + 1)} \frac{\Gamma_{\text{entr}}\Gamma_{\text{exit}}}{\Gamma_{\text{tot}}}. \quad (11)$$

Here, T_9 is the temperature in gigakelvin, M_i is the atomic mass in u of participating nucleus 0 or 1, E_r is the resonance energy in megaelectronvolts, $\omega\gamma$ is the resonance strength in megaelectronvolts, J, j_p, and j_t are the spins of resonance, projectile, and target nucleus, respectively, and Γ_{entr}, Γ_{exit}, and Γ_{tot} are the partial widths of the entrance channel, exit channel, and the total widths, respectively. The Monte Carlo samplings mentioned in Section 2 were conducted to obtain the nuclear inputs for the reaction rate calculations in Equations (10) and (11). For each temperature on a grid ranging from 0.1–2.0 GK (see

Table 4), each rate was calculated 10^5 times with this Monte Carlo sampling procedure described above.

Figure 3 shows histograms, which can also be interpreted as the probability density functions, of the ^{59}Cu$(p,\alpha)^{56}$Ni and ^{59}Cu$(p,\gamma)^{60}$Zn reaction rates at a low temperature, $T_9 = 0.4$. The histogram of the ^{59}Cu$(p,\alpha)^{56}$Ni reaction rate (right panel) has a long tail on the low rate side; these tails are most prevalent at low temperatures for this reaction. For this analysis, it was sufficient to cut off these tails at the 0.099 and 0.999 quantiles at a 90% confidence level over the entire temperature range. As the histogram of the ^{59}Cu$(p,\gamma)^{60}$Zn reaction rate does not exhibit a long tail, the 0.05 and 0.95 quantiles were chosen. The reaction rates are given in Table 4. To test the stability of the results, a few more runs of the entire calculation were performed, which showed the low, median, and high reaction rates were reproducible within $\sim$5%.
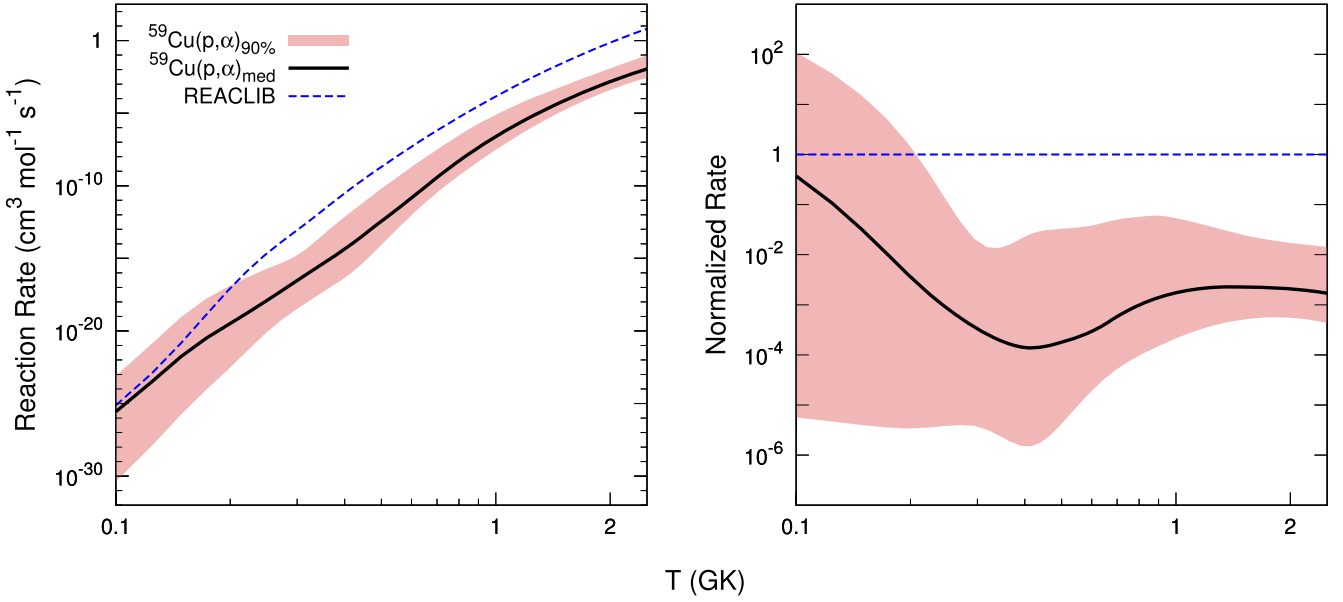
Figure 4. The ^{59}Cu$(p,\alpha)^{56}$Ni reaction rate as a function of temperature (gigakelvin). The left panel shows the rate in units of cubic centimeters per mole per second, while the right panel shows the rate normalized to the one from REACLIB (Cyburt et al. 2010).

Figure 5. The ^{59}Cu$(p,\gamma)^{60}$Zn reaction rate as a function of temperature (gigakelvin). The left panel shows the rate in units of cubic centimeters per mole per second, while the right panel shows the rate normalized to the one from REACLIB (Cyburt et al. 2010).
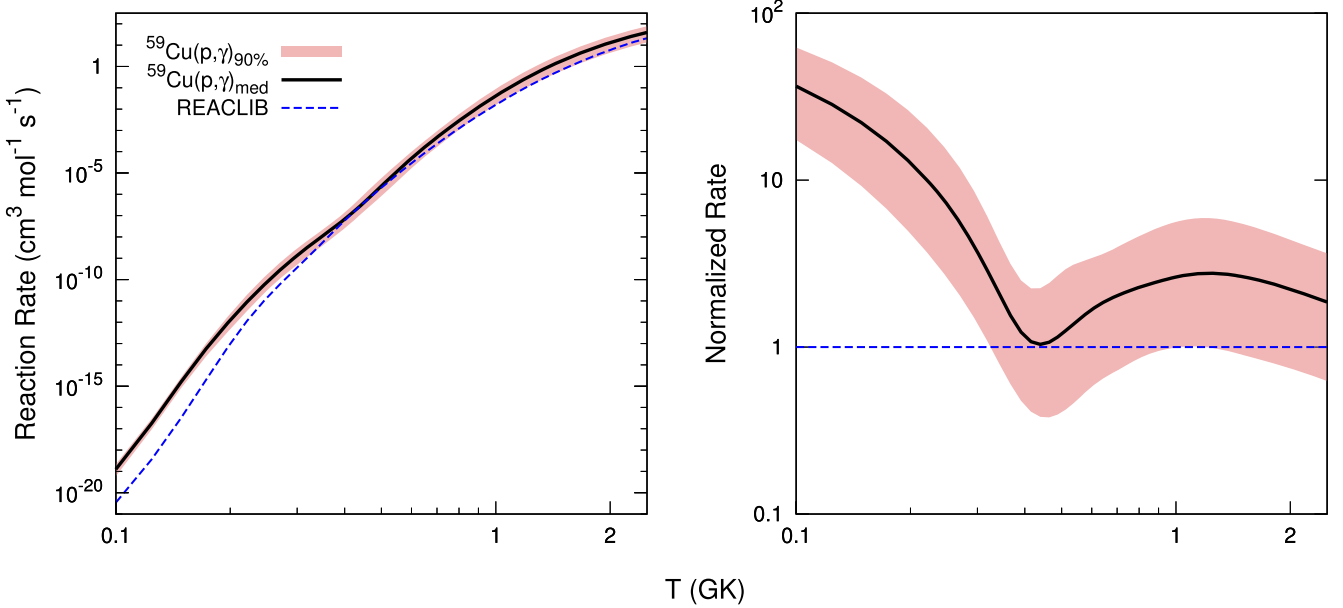
The reaction rates are plotted as a function of temperature in Figures 4 and 5. The ^{59}Cu$(p,\gamma)^{60}$Zn reaction rate has a narrow uncertainty range compared to the ^{59}Cu$(p,\alpha)^{56}$Ni rate because the proton and γ widths were obtained from the shell model, whereas the α widths were randomly sampled through the Porter–Thomas distribution. The rates from REACLIB (Cyburt et al. 2010) are also plotted as a reference, which were calculated using the statistical code NON-SMOKER (Rauscher & Thielemann 2000). The right panels of the figures show the rates normalized to those from REACLIB. The ^{59}Cu$(p,\alpha)^{56}$Ni reaction shows large discrepancies except in the low temperature region, $T_9 \lesssim 0.2$. The high ^{59}Cu$(p,\alpha)^{56}$Ni rate at $T_9 \gtrsim 0.3$ is lower than the REACLIB ^{59}Cu$(p,\alpha)^{56}$Ni rate by approximately two orders of magnitude, while the median rate is lower by approximately three orders of magnitude. The high and

median rates of ^{59}Cu$(p,\gamma)^{60}$Zn are higher than the corresponding REACLIB rate over the entire temperature range. Although the low rate is lower at temperatures higher than $T_9 \sim 0.3$, the factor of difference is smaller than 3. Our new reaction rates have differences from their respective REACLIB rates that are outside the range of variations implemented in the sensitivity studies of Parikh et al. (2008), Cyburt et al. (2016), and Meisel et al. (2019), except for the ^{59}Cu$(p,\alpha)^{56}$Ni rate at $T_9 \sim 0.1$.

The reduction of our ^{59}Cu$(p,\alpha)^{56}$Ni reaction rate compared to the REACLIB rate primarily originates from the strong selection rule on the α transitions to ^{56}Ni, a doubly magic nucleus, while parameters such as the alpha reduced width and total width also contribute. The penetration factors in Equation (4) are highly dependent on the penetration (decay)

6

energy and angular momentum transfer, l-value. Table 2 shows a large Q-value difference between the ground and first excited states of ^{56}Ni, which directly indicates a difference in the penetration energies. This implies that the transition to the ground state of ^{56}Ni dominates the alpha width. However, as the ground state is a 0^+ state, the selection rule does not allow transitions from odd $(-)$ parity states with l = even and even $(+)$ parity with l = odd. Additionally, the 0^+ state only allows a high l-value, unlike nonzero spin states because of the selection rule, $|J_i - J_f| \leqslant l \leqslant |J_i + J_f|$. These selection rules significantly lowered the penetration factors, and correspondingly, the rate of the ^{59}Cu$(p,\alpha)^{56}$Ni reaction.

The new rates and their uncertainties result in a NiCu cycle that is weaker than that resulting from REACLIB rates. The strength of the NiCu cycle can be characterized by the ratio of the ^{59}Cu$(p,\alpha)^{56}$Ni rate to the ^{59}Cu$(p,\gamma)^{60}$Zn rate, $N_A \langle \sigma v \rangle_{p,\alpha} / N_A \langle \sigma v \rangle_{p,\gamma}$. A ratio above 1 implies a strong NiCu cycle, corresponding to a reaction flow primarily cycling down to lower masses, whereas a ratio below 1 implies a weak NiCu cycle, corresponding to a reaction flow primarily proceeding up to higher masses and escaping the cycle. The previous sensitivity studies varied the reaction rates to reach the cycle strength of 1 at a temperature $T_9 < 2$. In Parikh et al. (2008), notable results were obtained by varying the NON-SMOKER rates (Rauscher & Thielemann 2000) by a factor of 10, creating a stronger NiCu cycle. Cyburt et al. (2016) and Meisel et al. (2019) varied the rates from REACLIB by a factor of 100, also creating a stronger NiCu cycle. Note that the rates from REACLIB (Cyburt et al. 2010), are based on those calculated with NON-SMOKER (Rauscher & Thielemann 2000). Figure 6 shows the estimated strength and its uncertainty in the present work, along with that from REACLIB (Rauscher & Thielemann 2000; Cyburt et al. 2010), and varied strengths by factors of 10 and 100. Because of the lower strength of the NiCu cycle with the new rates, we anticipate that the reaction flow in XRBs will primarily proceed to higher masses rather than returning to ^{56}Ni.

4. Type I X-Ray Bursts Model Construction

To estimate the impact of the NiCu cycle strength on Type I XRB nucleosynthesis, we performed simulations with Modules for Experiments in Stellar Astrophysics (MESA), a one-dimensional stellar evolution code (Paxton & Bildsten 2011; Paxton et al. 2013, 2015, 2018, 2019). The specific parameters for the model were adopted from Meisel (2018), which optimized model parameters to best reproduce the *clocked buster* GS 1826-24 (Heger et al. 2007; Galloway et al. 2008; Galloway 2020). The accretion matter composed of the hydrogen mass fraction $X = 0.70$, helium mass fraction $Y = 0.28$, and metallicity $Z = 0.02$ onto a neutron star with a mass $M_{NS} = 1.4\ M_\odot$ and radius $R_{NS} = 11.2$ km was implemented, at a mass accretion rate of $M_{acc} = 2.98 \times 10^{-9} M_\odot$ yr^{-1}. The solar metallicity of Grevesse & Sauval (1998) was adopted for the distribution of the metals. The nuclear reaction network was based on the network of Fisker et al. (2008), which is composed of 304 isotopes up to ^{107}Te. The luminosity at the base of the neutron star envelope was set to $L = 1.81 \times 10^{34}$ erg s^{-1} for the base heating $Q_b = 0.1$ MeV u^{-1}. More detailed descriptions of the model and MESA can be found in Meisel (2018) and in Paxton et al. (2015).

REACLIB (Cyburt et al. 2010), version 2.2 was used as the base library of the reaction rates. Four different models whose
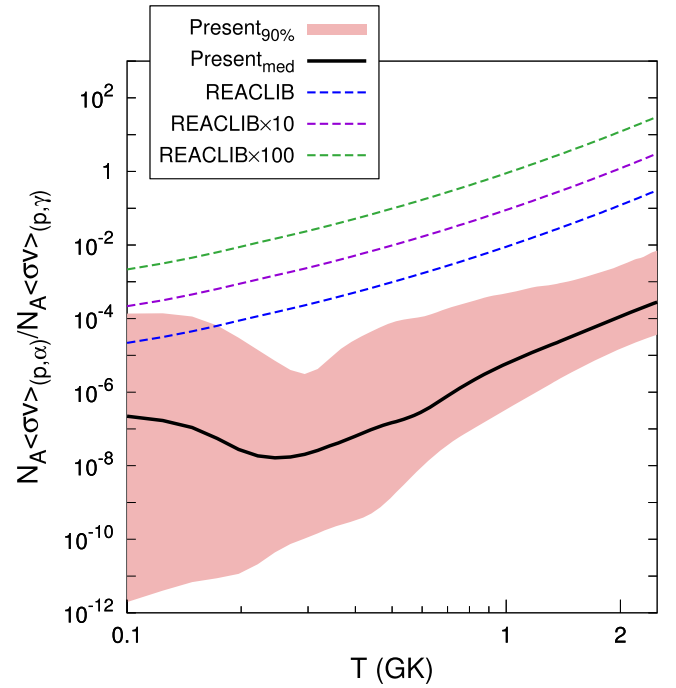

Figure 6. Strength of the NiCu cycle as a function of temperature (gigakelvin). The red band is obtained by setting the lower limit as the ratio of the low ^{59}Cu $(p,\alpha)^{56}$Ni and high ^{59}Cu$(p,\gamma)^{60}$Zn rates and the upper limit as the ratio of the high ^{59}Cu$(p,\alpha)^{56}$Ni and low ^{59}Cu$(p,\gamma)^{60}$Zn rates. The cycle strength by REACLIB and variations employed in the previous sensitivity studies are also plotted.

inputs differ only on the ^{59}Cu$(p,\alpha)^{56}$Ni and ^{59}Cu$(p,\gamma)^{60}$Zn reaction rates were computed: Model R with the rates from the base library, Model W with the low and high rates of the ^{59}Cu$(p,\alpha)^{56}$Ni and ^{59}Cu$(p,\gamma)^{60}$Zn reactions, respectively, from Table 4, Model M with the median and median rates, and Model S with the high and low rates, along with the corresponding reverse rates, which were calculated using the Computational Infrastructure for Nuclear Astrophysics (Smith et al. 2006, 2008). These particular rate combinations were chosen so that Models W, M, and S would have a weak, intermediate, and strong cycle strengths, respectively.

The luminosity profile for Model M is shown in Figure 7. A total of 12 bursts was simulated for each model. The first burst occurs in a fresh environment where ashes from previous bursts are absent, unlike subsequent bursts. It usually exhibits different properties compared to the others, such as higher luminosity (Woosley et al. 2004; Meisel 2018). In this work, mainly the later bursts were considered, where the bursts show similar behaviors to each other.

5. Results and Discussion

General burst properties, such as the peak luminosity L_{peak}, temperature T_{peak}, and recurrence time τ_{rec}, were extracted for the four models, as summarized in Table 5. The average properties of the 11 bursts, excluding the first burst, are presented with their standard deviations for each model. The properties of the first burst are also presented separately. Little differences were obtained between the properties of the four models. For the later bursts, the peak luminosity $L_{peak} \sim 1.8 \times 10^{38}$ erg s^{-1}, temperature $T_{peak} \sim 1.1$ GK, and recurrence time $\tau_{rec} \sim 2.5$ hr were obtained for the four models. T_{peak} and τ_{rec} were lying within the standard deviations from each other. For
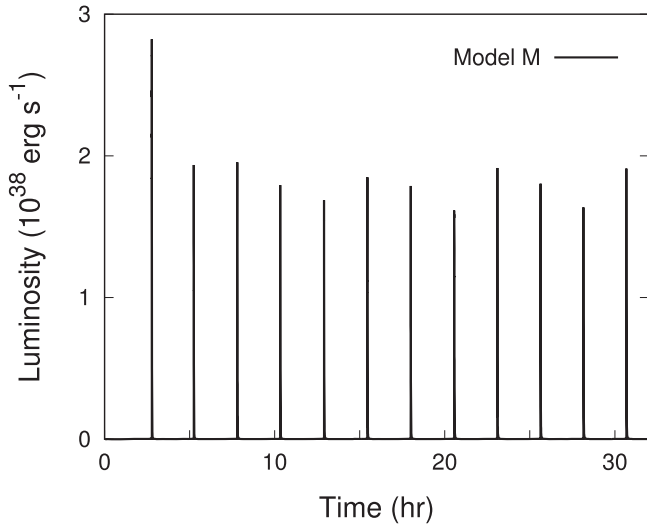
Figure 7. Luminosity profile for the 12 bursts from Model M (not redshifted). The accretion luminosity is not included in the profile.

Table 5
Summary of the General Burst Properties

Model	L_{peak} (10^{38} erg s^{-1})	T_{peak} (GK)	τ_{rec} (hr)
R First	2.74	1.11	2.46
R Later	1.87 ± 0.16	1.06 ± 0.01	2.53 ± 0.02
W First	2.71	1.12	2.42
W Later	1.83 ± 0.12	1.06 ± 0.01	2.54 ± 0.02
M First	2.82	1.12	2.47
M Later	1.81 ± 0.14	1.06 ± 0.01	2.54 ± 0.02
S First	2.87	1.12	2.49
S Later	1.82 ± 0.10	1.06 ± 0.01	2.54 ± 0.03

Note. "First" and "Later" mean the first and later 11 bursts, respectively; the mean value and standard deviation of the Later bursts are tabulated. τ_{rec} of the first burst represents the recurrence time between the first and second bursts. The redshift is not considered in the table.

L_{peak}, 2%–3% differences between the models were obtained. The first bursts had higher peak luminosities and temperatures with shorter recurrence times than the later bursts. The differences of the first burst properties between the four models were less than 6%.

The averages of the 11 light curves from Models R, W, and S are plotted in Figure 8, where the shaded areas represent the standard deviations. The one from Model M is also plotted in each panel as a reference for the light-curve shape comparison, where its average and standard deviation are presented as black solid and dashed lines, respectively. Note that the difference between Models M and R (Figure 8(a)) represents the influence of the cycle strength with the new rates compared to the strength with the previous rates. The differences between Models W and M, and between Models S and M (Figures 8(b) and (c), respectively) represent the influence of the uncertainty (the weakest and strongest variations) of our estimated strength of the NiCu cycle. Each light curve was linearly interpolated using the recorded time points from the simulation. The peak locations of the light curves are all aligned at a time equal to zero in the figure.

No significant differences were obtained between the light-curve shapes of the four models. To quantify the differences in the light curves from the four models, as has been done in
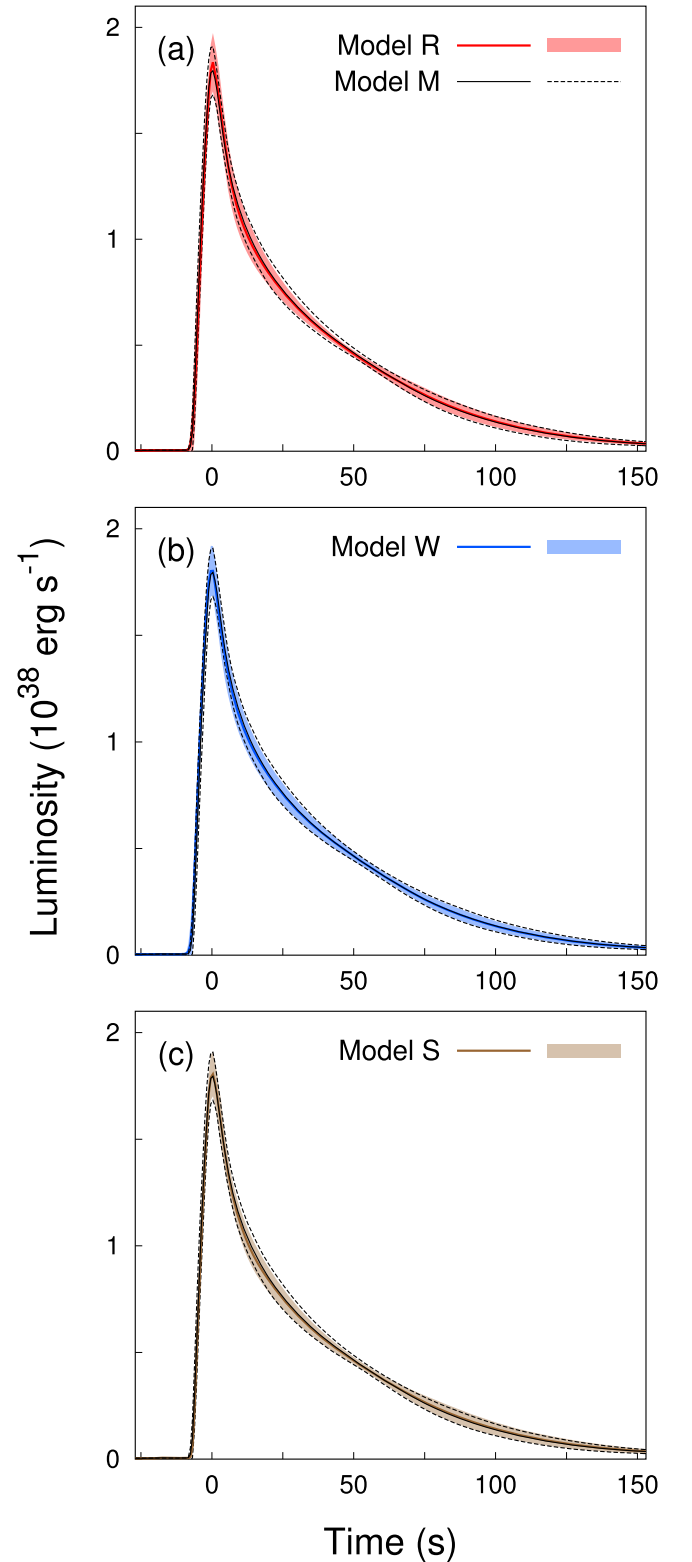
Figure 8. Light-curve shapes from Models R, W, and S, with the one from Model M as a reference. The averages and standard deviations of the light curves, excluding the first burst, from Models R, W, and S are presented as solid lines and bands. Those from Model M are presented as black solid and dashed lines.

Cyburt et al. (2016), the following quantity is defined:

$$\kappa_{ij} = \int_{burst} |\langle L_i \rangle - \langle L_j \rangle| \, dt, \qquad (12)$$

Table 6
Mass Fractions of the Ashes Obtained from the Four Models

A	Model R	Model W	Model M	Model S
4	9.19×10^{-4}	9.11×10^{-4}	9.23×10^{-4}	9.04×10^{-4}
12	2.34×10^{-3}	2.12×10^{-3}	2.12×10^{-3}	2.26×10^{-3}
16	1.53×10^{-5}	1.44×10^{-5}	1.46×10^{-5}	1.56×10^{-5}
20	1.70×10^{-5}	1.59×10^{-5}	1.57×10^{-5}	1.69×10^{-5}
24	1.27×10^{-4}	1.27×10^{-4}	1.15×10^{-4}	1.29×10^{-4}
25	1.01×10^{-7}	9.04×10^{-8}	8.61×10^{-8}	9.89×10^{-8}
27	2.63×10^{-7}	2.36×10^{-7}	2.41×10^{-7}	2.53×10^{-7}
28	9.72×10^{-3}	9.10×10^{-3}	9.05×10^{-3}	9.49×10^{-3}
29	1.33×10^{-5}	1.45×10^{-5}	1.26×10^{-5}	1.39×10^{-5}
30	3.70×10^{-4}	3.38×10^{-4}	3.48×10^{-4}	3.67×10^{-4}
31	1.82×10^{-3}	1.73×10^{-3}	1.68×10^{-3}	1.77×10^{-3}
32	8.12×10^{-2}	8.26×10^{-2}	8.33×10^{-2}	8.18×10^{-2}
33	6.44×10^{-3}	6.52×10^{-3}	6.39×10^{-3}	6.55×10^{-3}
34	9.09×10^{-3}	8.70×10^{-3}	8.35×10^{-3}	8.64×10^{-3}
35	4.73×10^{-3}	4.56×10^{-3}	4.36×10^{-3}	4.66×10^{-3}
36	7.95×10^{-3}	7.98×10^{-3}	8.03×10^{-3}	8.18×10^{-3}
37	1.09×10^{-3}	1.13×10^{-3}	1.10×10^{-3}	1.15×10^{-3}
38	4.42×10^{-3}	4.20×10^{-3}	3.91×10^{-3}	4.21×10^{-3}
39	4.32×10^{-3}	3.89×10^{-3}	3.61×10^{-3}	4.01×10^{-3}
40	2.13×10^{-3}	2.04×10^{-3}	2.03×10^{-3}	2.18×10^{-3}
41	5.30×10^{-5}	5.81×10^{-5}	5.87×10^{-5}	6.02×10^{-5}
42	5.75×10^{-4}	5.37×10^{-4}	4.99×10^{-4}	5.36×10^{-4}
43	3.43×10^{-4}	3.04×10^{-4}	2.91×10^{-4}	3.17×10^{-4}
44	5.29×10^{-4}	5.00×10^{-4}	4.79×10^{-4}	5.12×10^{-4}
45	3.84×10^{-4}	3.61×10^{-4}	3.59×10^{-4}	3.59×10^{-4}
46	1.09×10^{-3}	9.64×10^{-4}	8.83×10^{-4}	9.95×10^{-4}
47	4.49×10^{-4}	3.90×10^{-4}	3.80×10^{-4}	4.16×10^{-4}
48	7.89×10^{-4}	7.58×10^{-4}	7.47×10^{-4}	7.87×10^{-4}
49	8.63×10^{-4}	8.12×10^{-4}	8.03×10^{-4}	8.48×10^{-4}
50	1.21×10^{-3}	1.09×10^{-3}	1.03×10^{-3}	1.13×10^{-3}
51	1.89×10^{-3}	1.68×10^{-3}	1.60×10^{-3}	1.77×10^{-3}
52	3.61×10^{-3}	3.66×10^{-3}	3.77×10^{-3}	3.77×10^{-3}
53	1.16×10^{-3}	1.18×10^{-3}	1.22×10^{-3}	1.20×10^{-3}
54	1.26×10^{-3}	1.20×10^{-3}	1.19×10^{-3}	1.25×10^{-3}
55	3.16×10^{-3}	3.00×10^{-3}	2.94×10^{-3}	3.11×10^{-3}
56	9.75×10^{-3}	8.49×10^{-3}	7.97×10^{-3}	8.93×10^{-3}
57	2.77×10^{-3}	2.90×10^{-3}	3.07×10^{-3}	2.95×10^{-3}
58	1.15×10^{-3}	1.18×10^{-3}	1.25×10^{-3}	1.22×10^{-3}
59	3.38×10^{-3}	1.61×10^{-3}	2.74×10^{-3}	5.20×10^{-3}
60	1.16×10^{-1}	1.13×10^{-1}	1.13×10^{-1}	1.12×10^{-1}
61	8.28×10^{-3}	8.84×10^{-3}	9.47×10^{-3}	8.58×10^{-3}
62	4.61×10^{-3}	4.89×10^{-3}	5.26×10^{-3}	4.74×10^{-3}
63	1.08×10^{-2}	1.14×10^{-2}	1.18×10^{-2}	1.11×10^{-2}
64	3.65×10^{-1}	3.71×10^{-1}	3.75×10^{-1}	3.68×10^{-1}
65	2.23×10^{-2}	2.22×10^{-2}	2.22×10^{-2}	2.26×10^{-2}
66	1.19×10^{-2}	1.21×10^{-2}	1.17×10^{-2}	1.19×10^{-2}
67	1.36×10^{-2}	1.37×10^{-2}	1.33×10^{-2}	1.38×10^{-2}
68	1.29×10^{-1}	1.29×10^{-1}	1.25×10^{-1}	1.27×10^{-1}
69	1.88×10^{-2}	1.87×10^{-2}	1.87×10^{-2}	1.92×10^{-2}
70	6.20×10^{-3}	6.05×10^{-3}	6.05×10^{-3}	6.23×10^{-3}
71	6.72×10^{-3}	6.45×10^{-3}	6.42×10^{-3}	6.69×10^{-3}
72	3.94×10^{-2}	3.85×10^{-2}	3.75×10^{-2}	3.82×10^{-2}
73	1.09×10^{-2}	1.09×10^{-2}	1.10×10^{-2}	1.12×10^{-2}
74	3.96×10^{-3}	3.84×10^{-3}	3.87×10^{-3}	4.01×10^{-3}
75	5.07×10^{-3}	4.92×10^{-3}	4.97×10^{-3}	5.14×10^{-3}
76	1.21×10^{-2}	1.17×10^{-2}	1.16×10^{-2}	1.19×10^{-2}
77	5.06×10^{-3}	5.12×10^{-3}	5.16×10^{-3}	5.26×10^{-3}
78	4.08×10^{-3}	4.05×10^{-3}	4.08×10^{-3}	4.22×10^{-3}
79	3.98×10^{-3}	3.98×10^{-3}	3.99×10^{-3}	4.13×10^{-3}
80	4.71×10^{-3}	4.62×10^{-3}	4.59×10^{-3}	4.75×10^{-3}
81	2.83×10^{-3}	2.95×10^{-3}	2.95×10^{-3}	2.99×10^{-3}
82	3.91×10^{-3}	4.12×10^{-3}	4.09×10^{-3}	4.16×10^{-3}
83	2.42×10^{-3}	2.60×10^{-3}	2.56×10^{-3}	2.60×10^{-3}
84	2.17×10^{-3}	2.25×10^{-3}	2.21×10^{-3}	2.29×10^{-3}
85	2.45×10^{-3}	2.71×10^{-3}	2.69×10^{-3}	2.66×10^{-3}

Table 6
(Continued)

A	Model R	Model W	Model M	Model S
86	2.10×10^{-3}	2.40×10^{-3}	2.36×10^{-3}	2.33×10^{-3}
87	2.15×10^{-3}	2.48×10^{-3}	2.46×10^{-3}	2.39×10^{-3}
88	1.02×10^{-3}	1.12×10^{-3}	1.12×10^{-3}	1.11×10^{-3}
89	1.59×10^{-3}	1.79×10^{-3}	1.83×10^{-3}	1.75×10^{-3}
90	4.87×10^{-4}	5.38×10^{-4}	5.48×10^{-4}	5.36×10^{-4}
91	4.26×10^{-4}	4.80×10^{-4}	5.00×10^{-4}	4.69×10^{-4}
92	3.25×10^{-4}	3.62×10^{-4}	3.76×10^{-4}	3.61×10^{-4}
93	3.02×10^{-4}	3.25×10^{-4}	3.40×10^{-4}	3.30×10^{-4}
94	1.01×10^{-3}	1.10×10^{-3}	1.16×10^{-3}	1.10×10^{-3}
95	3.27×10^{-5}	3.23×10^{-5}	2.93×10^{-5}	2.98×10^{-5}
96	1.24×10^{-4}	1.34×10^{-4}	1.41×10^{-4}	1.33×10^{-4}
97	1.59×10^{-4}	1.71×10^{-4}	1.80×10^{-4}	1.68×10^{-4}
98	1.82×10^{-4}	1.94×10^{-4}	2.02×10^{-4}	1.86×10^{-4}
99	1.42×10^{-4}	1.61×10^{-4}	1.63×10^{-4}	1.45×10^{-4}
100	9.09×10^{-5}	1.08×10^{-4}	1.07×10^{-4}	9.25×10^{-5}
101	6.47×10^{-5}	7.81×10^{-5}	7.61×10^{-5}	6.29×10^{-5}
102	3.41×10^{-5}	4.23×10^{-5}	3.97×10^{-5}	3.13×10^{-5}
103	1.61×10^{-5}	2.12×10^{-5}	1.88×10^{-5}	1.40×10^{-5}
104	4.11×10^{-6}	5.90×10^{-6}	4.90×10^{-6}	3.40×10^{-6}
105	2.81×10^{-7}	4.73×10^{-7}	3.55×10^{-7}	2.25×10^{-7}

Note. Only those higher than 10^{-9} are listed.

where i (j) represents Models R, W, M, or S. For j = Model M, we obtained $\kappa_{ij} = 1.15 \times 10^{38}$ and 1.09×10^{38} erg s^{-1} for i = Models W and S, respectively. These integrated differences should be compared to the total integrated luminosity for Model M, 6.98×10^{39} erg s^{-1}. The variation in the strength of our estimate of the NiCu cycle therefore causes fractional changes of $\sim 1.6\%$ in the integrated luminosity. For i = Model R, we obtained $\kappa_{ij} = 1.15 \times 10^{38}$ erg s^{-1}, showing a small variation between the light curve using the old rates in comparison to our new rates. Our new estimate of the strength causes fractional changes of $\sim 1.6\%$ compared to the previous one. The magnitudes of κ are rather smaller than those reported by Cyburt et al. (2016), where the quantities were 6.4×10^{38} and 5.1×10^{38} erg s^{-1} for their variations of the $^{59}Cu(p,\alpha)^{56}Ni$ and $^{59}Cu(p,\gamma)^{60}Zn$ rates, respectively. Note that, also, the differences between the light curves are smaller than the standard deviation of each light curve. The minor differences in the light curves between Models W, M, and S indicate that, although the uncertainty of the estimated strength is high, interpretations of observational data are little affected.

The mass fractions, $X(A)$, of the burst ashes were obtained from the zones facing little nuclear burning with stabilized compositions, as has been similarly done in Cyburt et al. (2016), Meisel & Deibel (2017), and Meisel et al. (2019). The compositions formed after each burst converged after four to six bursts for the four models. They were extracted at the time with the lowest luminosity after the 12th burst. The mass fractions of the compositions exceeding 10^{-9} are listed in Table 6.

Except for the mass fraction of $A = 59$, the compositions from the models had no notably different mass fractions. Although the differences in the cycle strength between the models are large, increments on the mass fractions of the heavy elements were found to be negligible. The average of the

changes in the mass fractions of $A > 59$ nuclei of Model M compared to that of Model R was a factor of ~1.06, where the corresponding change between Model W and Model M was a factor of ~1.00. Simulations using the rates from REACLIB already result in very weak cycling: the fraction of nuclides burned through $^{59}\text{Cu}+p$ returning to ^{56}Ni is only about 10^{-5}–10^{-2} in the relevant temperature range $T \lesssim 1.1$ GK as shown in Figure 6, meaning that over 99% of the material is processed to higher masses. The REACLIB rates, therefore, already had nearly complete processing of nuclides up to higher masses. With our new rates, the cycle strength is even weaker, with less than 10^{-4} over this temperature range being recycled, meaning that more than 99.99% is processed up to higher masses. This small change in the reaction flow to higher masses is not statistically significant. The importance of our study is not in the change of final abundances, but rather in determining a rate based more firmly on experimental measurements, and on quantifying the uncertainties of the rates and their impact on XRB light curves and nucleosynthesis.

Note that a particular abundance can be affected by the two reactions individually, regardless of the cycle strength. This can be seen in the mass number $A = 59$. The ratios of the mass fractions between the models are $X(A)_R/X(A)_M = 1.24$, $X(A)_W/X(A)_M = 0.59$, and $X(A)_S/X(A)_M = 1.90$, where subscripts represent models. Although Model S does not have the strongest or weakest strength among the four models, the mass fraction of $A = 59$ was the highest. This occurs because the individual contribution from the $^{59}\text{Cu}(p,\gamma)^{60}\text{Zn}$ reaction to the synthesis of $A = 59$ significantly exceeds the contribution from the $^{59}\text{Cu}(p,\alpha)^{56}\text{Ni}$ reaction. Both reactions basically destroy ^{59}Cu. However, for the $^{59}\text{Cu}(p,\alpha)^{56}\text{Ni}$ reaction, the cyclical reaction flow can produce additional $A = 59$ isotopes. Additionally, as the flow at ^{59}Cu mainly goes through $^{59}\text{Cu}(p,\gamma)^{60}\text{Zn}$, the impact of the $^{59}\text{Cu}(p,\gamma)^{60}\text{Zn}$ reaction is greater on the $A = 59$ abundances. Model S has the weakest $^{59}\text{Cu}(p,\gamma)^{60}\text{Zn}$ reaction rate among the four models at temperatures $T_9 \gtrsim 0.3$. This resulted in the least destruction of $A = 59$ nuclides, and therefore the highest mass fraction of $A = 59$.

6. Conclusion and Remaining Work

In this study, the $^{59}\text{Cu}(p,\alpha)^{56}\text{Ni}$ and $^{59}\text{Cu}(p,\gamma)^{60}\text{Zn}$ thermonuclear reaction rates were critically assessed in the temperature range relevant to Type I XRBs. Our new rates incorporate experimental measurements, and utilize a Monte Carlo approach to quantify the rate uncertainties. We found a low $^{59}\text{Cu}(p,\alpha)^{56}\text{Ni}$ reaction rate and weak NiCu cycle strength mainly due to the strong selection rule on the α transition. The new ratio between the values of these two reaction rates, $N_A\langle\sigma v\rangle_{p,\alpha}/N_A\langle\sigma v\rangle_{p,\gamma}$, clearly indicates a NiCu cycle strength that is even weaker than previously estimated: less than 1 part in 10^4 of material burned through ^{59}Cu $+ p$ is recycled back to ^{56}Ni, with the rest being processed to higher masses. Our XRB model simulations with the new rates and their uncertainties show that variations of the estimated strength of the NiCu cycle within our newly assessed uncertainties do not strongly influence the model predictions of the general burst properties, light curve, and composition of the ashes of the burst, except for the mass fraction of $A = 59$ nuclides. An insignificant effect on the enhancement of the heavy element production was obtained even with this new weaker cycle strength. Only a few percent differences were obtained for the burst properties, light curves, and production on the heavy nuclei between the models.

Estimations of the impact of the NiCu cycle on other hosting environments are required, as they can create different burst properties that strongly affect the nucleosynthesis processes such as the temperature. The burst model implemented in this work has the peak temperature just above 1 GK. However, some models with different astrophysical inputs, such as accretion rates and neutron star properties, achieve a higher peak temperature of up to 2 GK (Schatz et al. 2001; Koike et al. 2004; Parikh et al. 2008, 2013). Therefore, the impact of the NiCu cycle strength and reaction rates on the burst models in other environments needs to be investigated.

Recent sensitivity studies of core-collapse supernovae (CCSNe) to nuclear reaction rates showed that the $^{59}\text{Cu}(p,\alpha)^{56}\text{Ni}$ and $^{59}\text{Cu}(p,\gamma)^{60}\text{Zn}$ reaction rate variations notably affect the production of γ-ray emitting isotopes (Hermansen et al. 2020; Subedi et al. 2020). As CCSNe also accompany the rp process, the NiCu cycle or individual reactions can affect the CCSNe model predictions. Reaction rate estimations for the CCSNe temperature, which is higher than the typical temperature of Type I XRBs, are required for the investigation.

To investigate these scenarios, it will be crucial to focus on the partial widths of levels in ^{60}Zn, where the uncertainties of the widths calculated by the shell model calculation could not be estimated. More experiments to constrain the partial widths, such as experiments using the β-delayed decay of ^{60}Ga, will effectively reduce the uncertainties. Additional energy state measurements with high energy resolution are required to find unknown resonance contributions. This can be achieved with nucleon transfer reactions such as the $^{58}\text{Ni}(^{3}\text{He},n)^{60}\text{Zn}$ reaction. Resonant states of low spins with high proton and low gamma widths can considerably contribute to the $^{59}\text{Cu}(p,\alpha)^{56}\text{Ni}$ reaction rate. Meanwhile, if the magnitudes of the contributions are about the same to both reactions, the NiCu cycle strength will not be strongly affected. Investigating nonresonant and direct reaction contributions will give more accurate reaction rates. Although direct measurements of the reaction cross sections are challenging for a wide range of the center of mass energy, the measurements on a few energy points will also considerably enhance the evaluation of the rates (Randhawa et al. 2021).

ORCID iDs

Chanhee Kim ⬤ https://orcid.org/0000-0002-4614-4793
Kyungyuk Chae ⬤ https://orcid.org/0000-0003-1819-079X
Kyujin Kwak ⬤ https://orcid.org/0000-0002-2304-7798
Michael Smith ⬤ https://orcid.org/0000-0002-4737-4099

References

Alford, W. P., Lindgren, R. A., Elmore, D., & Boyd, R. N. 1975, NuPhA, 243, 269
Boucenna, A., Kraus, L., Linck, I., & Chan, T. U. 1990, PhRvC, 42, 1297
Browne, E., & Tuli, J. K. 2013, NDS, 114, 1849

Cyburt, R. H., Amthor, A. M., Ferguson, R., et al. 2010, ApJS, 189, 240
Cyburt, R. H., Amthor, A. M., Heger, A., et al. 2016, ApJ, 830, 55
de Angelis, G., Fahlander, C., Gadea, A., et al. 1998, NuPhA, 630, 426
Evers, D., Assmann, W., Rudolph, K., Skorka, S. J., & Sperr, P. 1974, NuPhA, 230, 109
Fisker, J. L., Schatz, H., & Thielemann, F.-K. 2008, ApJS, 174, 261
Galloway, D. K., in 't Zand, J., Chenevez, J., et al. 2020, ApJS, 249, 32
Galloway, D. K., Muno, M. P., Hartman, J. M., Psaltis, D., & Chakrabarty, D. 2008, ApJS, 179, 360
Garrett, P. E., Lehmann, H., Jolie, J., et al. 2001, PhRvC, 64, 024316
Gilbert, A., & Cameron, A. G. W. 1965, CaJPh, 43, 1446
Greenfield, M. B., Bingham, C. R., Newman, E., & Saltmarsh, M. J. 1972, PhRvC, 6, 1756
Grevesse, N., & Sauval, A. J. 1998, SSRv, 85, 161
Heger, A., Cumming, A., Galloway, D. K., & Woosley, S. E. 2007, ApJL, 671, L141
Hermansen, K., Couch, S. M., Roberts, L. F., Schatz, H., & Warren, M. L. 2020, ApJ, 901, 77
Honma, M., Otsuka, T., Mizusaki, T., & Hjorth-Jensen, M. 2009, PhRvC, 80, 064323
Iliadis, C. 1997, NuPhA, 618, 166
Iliadis, C. 2015, Nuclear Physics of Stars (New York: Wiley)
Joss, P. C. 1977, Natur, 270, 310
Junde, H., Su, H., & Dong, Y. 2011, NDS, 112, 1513
Kamermans, R., Jongsma, H. W., van der Spek, J., & Verheul, H. 1974, PhRvC, 10, 620
Koike, O., Hashimoto, M.-A., Kuromizu, R., & Fujimoto, S. I 2004, ApJ, 603, 242
Koning, A., Hilaire, S., & Goriely, S. 2017, TALYS-1.9 User Manual
Lane, A. M., & Thomas, R. G. 1958, RvMP, 30, 257
Lewin, W. H. G., van Paradijs, J., & Taam, R. E. 1993, SSRv, 62, 223
Long, A. M., Adachi, T., Beard, M., et al. 2017, PhRvC, 95, 055803
Long, A. M., Adachi, T., Beard, M., et al. 2018, PhRvC, 97, 054613
Longland, R., Iliadis, C., Champagne, A. E., et al. 2010, NuPhA, 841, 1
Mazzocchi, C., Janas, Z., Döring, J., et al. 2001, EPJA, 12, 269
Meisel, Z. 2018, ApJ, 860, 147
Meisel, Z., & Deibel, A. 2017, ApJ, 837, 73
Meisel, Z., Merz, G., & Medvid, S. 2019, ApJ, 872, 84
Özdoğan, H., Üncü, Y. A., Şekerci, M., & Kaplan, A. 2021, Appl. Radiat. Isot., 169, 109583
Parikh, A., José, J., Iliadis, C., Moreno, F., & Rauscher, T. 2009, PhRvC, 79, 045802

Parikh, A., José, J., Moreno, F., & Iliadis, C. 2008, ApJS, 178, 110
Parikh, A., José, J., Sala, G., & Iliadis, C. 2013, PrPNP, 69, 225
Paxton, B., Bildsten, L., Dotter, A., et al. 2011, ApJS, 192, 3
Paxton, B., Cantiello, M., Arras, P., et al. 2013, ApJS, 208, 4
Paxton, B., Marchant, P., Schwab, J., et al. 2015, ApJS, 220, 15
Paxton, B., Schwab, J., Bauer, E. B., et al. 2018, ApJS, 234, 34
Paxton, B., Smolec, R., Schwab, J., et al. 2019, ApJS, 243, 10
Pogrebnyak, I., Howard, C., Iliadis, C., Longland, R., & Mitchell, G. E. 2013, PhRvC, 88, 015808
Porter, C. E., & Thomas, R. G. 1956, PhRv, 104, 483
Pougheon, F., Roussel, P., Colombani, P., Doubre, H., & Roynette, J. C. 1972, NuPhA, 193, 305
Rahman, A. R., & Zubair, M. A. 2020, Appl. Radiat. Isot., 166, 109429
Randhawa, J. S., Kanungo, R., Refsgaard, J., et al. 2021, PhRvC, 104, L042801
Rauscher, T., & Thielemann, F.-K. 2000, ADNDT, 75, 1
Schatz, H., Aprahamian, A., Barnard, V., et al. 2001, PhRvL, 86, 3471
Schatz, H., & Ong, W.-J. 2017, ApJ, 844, 139
Schatz, H., & Rehm, K. 2006, NuPhA, 777, 601
Schiller, A., Bjerve, A., Guttormsen, M., et al. 2001, PhRvC, 63, 021306
Schubank, R. B., Cameron, J. A., & Janzen, V. P. 1989, PhRvC, 40, 2310
Shimizu, N. 2013, arXiv:1310.5431
Shimizu, N., Mizusaki, T., Utsuno, Y., & Tsunoda, Y. 2019, CoPhC, 244, 372
Smith, M. S., Cyburt, R., Schatz, H., et al. 2008, in AIP Conf. Ser. 1016, Origin of Matter and Evolution of Galaxies, ed. T. Suda et al. (Melville, NY: AIP), 466
Smith, M. S., Lingerfelt, E. J., Scott, J. P., et al. 2006, APS Meeting Abstracts, L8.002
Subedi, S. K., Meisel, Z., & Merz, G. 2020, ApJ, 898, 5
Svensson, C. E., Rudolph, D., Baktash, C., et al. 1999, PhRvL, 82, 3400
van Wormer, L., Görres, J., Iliadis, C., Wiescher, M., & Thielemann, F. K. 1994, ApJ, 432, 326
Wallace, R. K., & Woosley, S. E. 1981, ApJS, 45, 389
Wang, M., Huang, W. J., Kondev, F. G., Audi, G., & Naimi, S. 2021, ChPhC, 45, 030003
Weber, D. J., Crawley, G. M., Benenson, W., Kashy, E., & Nann, H. 1979, NuPhA, 313, 385
Weinberg, N. N., Bildsten, L., & Schatz, H. 2006, ApJ, 639, 1018
Weisskopf, V., & Blatt, J. 1954, Theoretical Nuclear Physics (New York: Wiley)
Winsborrow, R. P. J., & Macefield, B. E. F. 1972, NuPhA, 182, 481
Woosley, S., Heger, A., & Cumming, A. E. A. 2004, ApJS, 151, 75
Woosley, S. E., & Taam, R. E. 1976, Natur, 263, 101